



# Enhancing obSTORM imaging performance with cubic spline PSF modeling

DONGHOON KOO,<sup>1,†</sup>  MINCHOL LEE,<sup>1,†</sup>  YOUNGSEOP LEE,<sup>1</sup> AND JEONGMIN KIM<sup>1,2,\*</sup> 

<sup>1</sup>Department of Applied Bioengineering, Graduate School of Convergence Science and Technology, Seoul National University, Seoul 08826, Republic of Korea

<sup>2</sup>Research Institute for Convergence Science, Seoul National University, Seoul 08826, Republic of Korea

<sup>†</sup>These authors contributed equally to this work.

\*jeomik@snu.ac.kr

**Abstract:** Oblique plane microscopy-based single molecule localization microscopy (obSTORM) has shown great potential for super-resolution imaging of thick biological specimens. Despite its compatibility with tissues and small animals, prior uses of the Gaussian point spread function (PSF) model have resulted in limited imaging resolution and a narrow axial localization range. This is due to the poor fit of the Gaussian PSF model with the actual PSF shapes in obSTORM. To overcome these limitations, we have employed cubic splines for a more accurate modeling of the experimental PSF shapes. This refined PSF model enhances three-dimensional localization precision, leading to significant improvements in obSTORM imaging of mouse retina tissues, such as an approximately 1.2 times increase in imaging resolution, seamless stitching of single molecules between adjacent optical sections, and a doubling of the sectional interval in volumetric obSTORM imaging due to the extended axial range of usable section thickness. The cubic spline PSF model thus offers a path towards more accurate and faster volumetric obSTORM imaging of biological specimens.

© 2023 Optica Publishing Group under the terms of the [Optica Open Access Publishing Agreement](#)

## 1. Introduction

Since its introduction in 2006, single molecule localization microscopy (SMLM) [1–3] has progressively advanced, becoming a key tool for imaging nanoscale structures in thin biological specimens, such as cultured cells [4,5] and tissue sections under 10  $\mu\text{m}$  thick [6,7]. Yet, the challenge of imaging thicker specimens with SMLM persists. The advent of lightsheet-based SMLM [8] has marked a turning point by confining illumination to the focal plane of the detection objective lens through side illumination from a separate lens. This method significantly reduces background fluorescence and minimizes optical aberrations when the refractive indices of the sample and immersion oil are matched, both crucial for achieving high-quality deep tissue imaging. More recent developments include the use of reflected lightsheet geometry [9–13], which can ease the need for orthogonal placement of the illumination objective or even enable a single objective configuration. However, these advancements necessitate specific sample holders or geometric arrangements, potentially complicating sample preparation or microscope use.

Oblique plane SMLM (obSTORM [14]) is an alternative approach to lightsheet SMLM that achieves oblique lightsheet imaging with a single objective configuration in sample space. This layout is fully compatible with standard microscopy specimens prepared on glass slides, making it convenient for accommodating laterally wide tissue sections and small animal samples, just like conventional microscope platforms. However, even with its capability to conduct SMLM imaging of thick biological specimens up to  $\sim 60 \mu\text{m}$  or thicker, obSTORM's imaging performance, encompassing localization precision, imaging resolution, and volumetric imaging speed, demands enhancements. This performance constraint primarily stems from the irregular behavior of the point spread function (PSF) in both its shape and size through focus [14], the

cause of which remains not fully understood. Specifically, the PSF shapes in obSTORM deviate from the conventionally-used Gaussian models, and the sensitivity of PSF size variations is constrained across the positive defocus range. Consequently, the previous use of the Gaussian PSF model for three-dimensional (3D) localization compromised localization precision, which in turn negatively affected imaging resolution. Moreover, the exclusion of single molecule data from the positive defocus range, due to suboptimal localization precision, effectively halved the volumetric imaging speed [14].

In this study, our goal is to enhance the 3D localization precision of single molecules in obSTORM by employing a refined PSF model based on cubic splines [15–18]. We construct this model from experimental PSF calibration images and evaluate its modeling accuracy and localization performance in comparison with the conventional Gaussian PSF model. Our approach aims to improve localization precision and extend the range for 3D localization to both defocus directions – an enhancement previously unattainable with obSTORM. We validate our method by conducting a comparative analysis of STORM images of a scanned fluorescent bead and mouse retina tissue sections, each reconstructed using the cubic spline and Gaussian PSF models, respectively.

## 2. Materials and methods

### 2.1. obSTORM system and PSF calibration

Figure 1 shows the simplified layout of obSTORM [14]. A water-immersion objective (O1; UPLSAPO 60XW/1.2, Olympus) is used to illuminate the specimen with an oblique sheet of light, and single molecule images along the  $xo$  oblique plane are refocused and reoriented to the focal plane of the remote objective (O2; MPlanApo 50×/0.95, Olympus) to be directly captured by the camera (Cascade II 512, Photometrics). The O1 objective has a numerical aperture (NA) of 1.2, and the angle ( $\alpha$ ) of oblique plane is primarily set at 45°. The setup uses a polarizing beam splitter and a quarter-wave plate to improve the isotropy of the vectorial PSF shape and double the light collection efficiency, compared to setups that use only a nonpolarizing beam splitter [14]. The total imaging magnification is  $\sim 110.7$  and the image pixel size in object space is 144.5 nm. For additional experimental details on the obSTORM system, refer to Ref. [14].

obSTORM employs a cylindrical lens positioned in front of the camera to introduce astigmatism into PSFs [4], enabling 3D localization with the third localization direction ( $z_o$ ) perpendicular to the oblique plane ( $xo$ ). For PSF calibration, a  $z_o$ -stack of PSF images of deep-red fluorescent beads (P7220, Invitrogen) is captured by moving the sample objective (O1) in the  $z$  direction with a 30 nm step size, which corresponds to a  $z_o$  interval of 21.2 nm calculated by  $z_o = z \cos \alpha$  [14]. As shown in Fig. 1, the experimental PSF shapes show asymmetry along the  $x$  and  $o$  axes, particularly at larger defocus values. The cause of this behavior has not been fully identified. We also note that, while only the beads on the coverslip were assessed, the PSF shapes were presumed consistent across the sample depth, given the refractive index match between the objective lens and the specimen in the aqueous STORM imaging buffer.

### 2.2. PSF modeling: Gaussian function vs. cubic spline

In previous obSTORM demonstrations, the PSF shape was approximated as a 2D Gaussian function:

$$h(x, o) = \frac{N}{2\pi\sigma_x\sigma_o} \exp\left(-\frac{(x - \mu_x)^2}{2\sigma_x^2} - \frac{(o - \mu_o)^2}{2\sigma_o^2}\right) + b, \quad (1)$$

where  $N$  represents the number of signal photons collected from a molecule,  $b$  represents the constant background (photons/pixel), and  $\sigma_i$  and  $\mu_i$  are the width and the center position of the pixelated PSF image in the  $i$  direction ( $i = x, o$ ), respectively [14]. The PSF shape was assumed to remain Gaussian across defocus ( $z_o$ ), except for changes in the PSF size. To construct a 3D

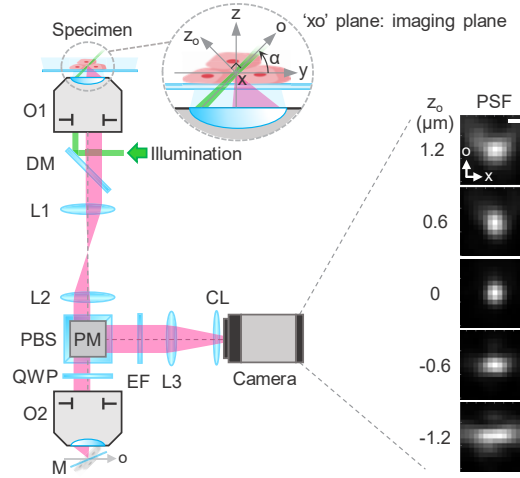


**Fig. 1.** Conceptual schematic of obSTORM. O, objective; DM, dichroic mirror; L, lens; PBS, polarizing beam splitter; PM, periscope mirror; QWP, quarter-wave plate; M, mirror; EF, emission filter; CL, cylindrical lens. The lenses L1, L2, and L3 have focal lengths of 200 mm, 180 mm, and 300 mm, respectively. Experimental PSF images (normalized to maximum intensity) at different defoci in the  $z_o$  direction are shown. Scale bar: 500 nm.

PSF model that captures the variations in PSF widths through focus, each PSF image from the measured 3D stack was fitted with the Gaussian function described above using MATLAB. The resulting PSF widths were then modeled using 8<sup>th</sup> order polynomials:

$$\sigma_x(z_o) = \sum_{i=0}^8 c_i z_o^i \text{ and } \sigma_o(z_o) = \sum_{i=0}^8 d_i z_o^i \quad (2)$$

Similarly, the lateral ( $xo$ ) shift of the PSF's central position through focus, influenced by the asymmetric pupil and PSF shapes about the  $x$  and  $o$  axes, was also extracted and modeled using 5<sup>th</sup> order polynomials for correction.

In contrast, cubic spline (or cspline) modeling offers the flexibility to model complex-shaped PSFs that may vary considerably across defocus. This adaptability arises from the approach of modeling each voxel of the 3D PSF using distinct piecewise 3<sup>rd</sup> order polynomials [15]. As introduced in Ref. [15], the PSF centered at  $(\mu_x, \mu_o, \mu_{z_o})$  can be modeled using cubic spline as

$$h_{i,j,k}(x, o) = \frac{N}{N_s} \sum_{l=0}^3 \sum_{m=0}^3 \sum_{n=0}^3 c_{i,j,k,l,m,n} \left( \frac{(x - \mu_x) - x_i}{p_x} \right)^l \left( \frac{(o - \mu_o) - o_j}{p_o} \right)^m \left( \frac{(\mu_{z_o} - z_k)}{p_z} \right)^n + b, \quad (3)$$

where each voxel (index:  $i, j, k$ ) of the 3D PSF is described by a set of 64 coefficients ( $c_{i,j,k,l,m,n}$ ), and the piecewise polynomials and their derivatives are continuous at voxel boundaries. Here,  $N_s$  denotes the normalization factor (obtained through 2D numerical integration of the cubic spline model image),  $x_i$ ,  $o_j$ , and  $z_k$  are the start positions of the voxel ( $i, j, k$ ) in the  $x$ ,  $o$ , and  $z_o$  directions, respectively, and  $p_x$ ,  $p_o$ , and  $p_z$  are the voxel sizes of the PSF stack in object space in each coordinate direction. Using the SMAP [16,17], we generated the cubic spline PSF model from four distinct experimental 3D PSF stacks.

### 2.3. STORM imaging data

To evaluate the relative performance of cubic spline and Gaussian PSF models in obSTORM imaging ( $\alpha = 45^\circ$ ), we referenced raw image datasets of 3D PSF stacks of dark-red beads and

volumetric single molecule images of mouse retina tissues from Ref. [14]. The 60  $\mu\text{m}$ -thick section of mouse retina tissue was immunostained with Alexa Fluor 647 to target the protein kinase C alpha (PKC $\alpha$ ) of rod bipolar cells. The volumetric STORM data comprises 10 optical sections, each spaced at a  $\sim 504$  nm  $z_o$ -step interval and containing 7,000-10,000 image frames recorded at a rate of 28 frames/s. For more comprehensive details concerning sample preparation and STORM image acquisition, refer to Ref. [14].

In addition, we utilized a STORM image dataset of a “straight line” specimen. This dataset was generated by slow scanning of a deep-red bead ( $\varnothing 180$  nm) over a  $\sim 3.6$   $\mu\text{m}$  range in the  $z$  direction, while capturing images of the moving bead over  $\sim 18,000$  frames at 50 frames/s. The illumination was adjusted to detect  $\sim 960$  photons from the bead per camera frame, a count which aligns with the average photon count of Alexa Fluor 647 molecules in obSTORM, as the light collection efficiency is  $\sim 25\%$  of that in conventional 1.4-NA STORM systems. In this instance, the average constant background was found to be  $\sim 17$  photons per pixel.

#### 2.4. Localization analysis and image reconstruction

We used SMAP software for the localization analysis based on the cspline PSF model, which utilizes maximum-likelihood estimation (MLE) for the estimator  $\hat{\theta} = [\mu_x, \mu_o, N, b, \mu_{z_o}]$ . One of the four 3D PSF stack datasets used for cspline PSF modeling was selected, and its PSF images were localized to calculate Cramér-Rao lower bound (CRLB) precision in SMAP based on the fitting result of  $\hat{\theta}$ . For comparison, we fitted the same bright bead data with the Gaussian PSF model and evaluated the CRLB precision by calculating the inverse of the Fisher information matrix using custom MATLAB codes for obSTORM [14]. The estimated CRLB precision values from both PSF models were scaled to correct for the dimensional distortion in the  $o$  direction caused by the cylindrical lens ( $\sim 1.19$ ) and an excess noise factor resulting from the EMCCD camera ( $\sim 1.41$ ).

To localize the single molecule data of the “straight line” bead and mouse retina sections, we used cspline and Gaussian fitting from SMAP and custom MATLAB codes, respectively. Once localization was achieved, we adjusted the data to correct for the cylindrical distortion present in the  $o$  direction. For mouse retina tissues, we filtered the localization data to exclude single molecules having CRLB precisions greater than 60 nm in  $xo$  or 130 nm in  $z_o$ . Lastly, we rendered the data for visualization through SMAP software.

### 3. Results and discussions

We evaluated the accuracy of the cubic spline PSF model in representing the structural features of obSTORM PSF shapes. As shown in Fig. 2, the cspline PSFs closely resembled the experimental PSF images of a deep-red bead across the entire  $z_o$  range of 2.4  $\mu\text{m}$ . The error images, which depict the differences between the experimental and model PSFs, revealed only small deviations at all  $z_o$  values, with a maximum pixel-wise intensity difference of 4.0% (relative to the peak intensity of one). This is a notable improvement over the previous Gaussian PSF models. Although the experimental PSFs had a Gaussian shape for  $-0.6 \mu\text{m} \leq z_o \leq 0.3 \mu\text{m}$ , the pixel-wise error remained as high as 10.8% (including 7.3% error even at focus,  $z_o = 0 \mu\text{m}$ ). The Gaussian PSF model could reasonably capture the change in PSF ellipticity at  $-1.2 \mu\text{m} \leq z_o \leq -0.9 \mu\text{m}$ , but the maximum error exceeded 21.8%. Moreover, for  $0.9 \mu\text{m} \leq z_o \leq 1.2 \mu\text{m}$ , the Gaussian model failed to represent the two upper tails of the PSF and had a larger PSF size than the experimental PSFs, resulting in a modeling error as large as 27.8%.

To further assess the effectiveness of the cubic spline PSF model over the Gaussian PSF model, we compared the CRLBs on localization precision calculated from the localization results of the bright bead images used for PSF calibration. The bright bead had a photon count of  $\sim 53,000$  photons and a constant background of  $\sim 182$  photons/pixel, when averaged over all  $z_o$  positions. As depicted in Fig. 3, the cspline PSF model demonstrated superior performance over the entire

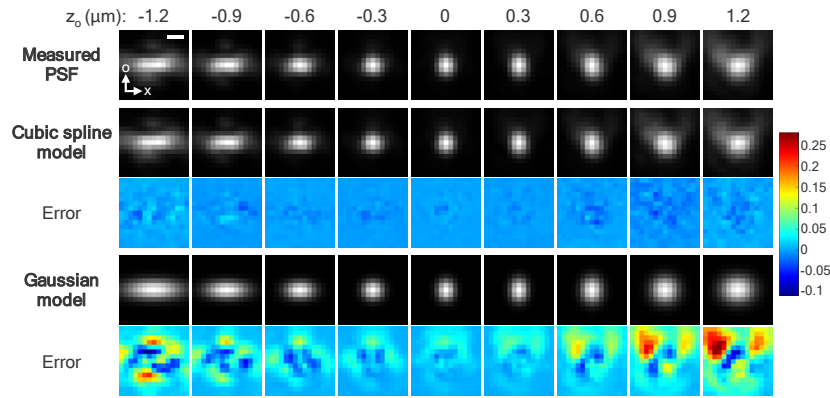


**Fig. 2.** Experimental PSF and its numerical models based on cubic spline and elliptical Gaussian function. The maximum intensity of the images was normalized to one. Errors represent pixel-wise difference between the measured and model PSFs. Scale bar: 500 nm.

$z_o$  range compared to the Gaussian model. In the  $x$  and  $o$  directions, the cubic spline PSF model improved the CRLB precision by approximately 1.1-1.6 times, depending on the  $z_o$  position (on average, 1.25 $\times$  and 1.16 $\times$  for all  $z_o$  in  $x$  and  $o$  directions, respectively), with a gradual improvement observed with increasing defocus to  $\pm 1.2 \mu\text{m}$ . This trend was quite consistent with the larger modeling errors observed with increasing defocus in Fig. 2.

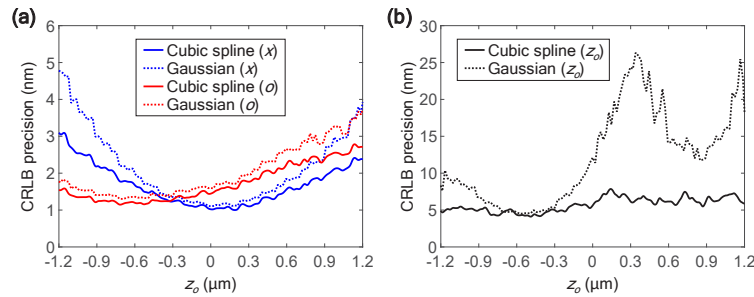


**Fig. 3.** Comparison of CRLBs on localization precision in (a)  $x$ ,  $o$ , and (b)  $z_o$  directions for a bright deep-red bead when localized using cubic spline and Gaussian PSF models.

The improvement in CRLB precision in the  $z_o$  direction varied significantly depending on the value of  $z_o$ , with an average improvement factor of 2.0 $\times$  for all  $z_o$  values. For  $-0.9 \mu\text{m} < z_o < -0.1 \mu\text{m}$ , the cubic spline PSF model provided minimal improvement in CRLB precision, with an improvement factor of about 1-1.5 times. This was due to the dramatic change in ellipticity in PSF shapes in this range, where PSF size was a reasonably good figure of merit for defining the axial position of  $z_o$ . Therefore, the previous obSTORM method restricted the working range for 3D localization to the negative defocus side ( $-1.0 \mu\text{m} \leq z_o \leq 0 \mu\text{m}$ ), given the poor localization precision from the Gaussian PSF model on the positive defocus side due to insensitive PSF size changes. In contrast, the cubic spline PSF model substantially improved  $z_o$  precision by about 2-4 times over positive  $z_o$  values by adeptly capturing minor PSF shape variations. Moreover, the cubic spline PSF model maintained relatively uniform CRLB precision in the  $z_o$  direction across the entire  $z_o$  range, including both ends ( $-1.2 \mu\text{m} < z_o < -0.9 \mu\text{m}$  and  $0.9 \mu\text{m} < z_o < 1.2 \mu\text{m}$ ), without any performance degradation seen with the Gaussian PSF model. Consequently, by



modeling the obSTORM PSF with a cubic spline, the full  $2.4\ \mu\text{m}$   $z_o$  range is expected to be utilizable.

As CRLB precision alone is not sufficient to explain SMLM imaging resolution, we also evaluated the imaging resolution by obtaining STORM images of a  $z$ -scanned bead. Ideally, the scanned bead should appear as a narrow straight line, with its width representing the imaging resolution. The bead was adjusted to a brightness level of approximately 960 photons, which is similar to the brightness of Alexa fluor 647 during obSTORM imaging. As shown in Figs. 4(a) and 4(b), the reconstructed STORM images using the cspline PSF model showed narrower linewidths over the entire  $z_o$  range, with particularly noticeable improvements in the positive defocus range. In  $xo$  plane view, the full width at half maximum (FWHM) linewidths of cross-sectional intensity profiles were found to be improved by  $1.6\times$ ,  $1.3\times$ , and  $1.3\times$  for three different  $z_o$  positions ( $-1.0$ ,  $0.3$ , and  $1.0\ \mu\text{m}$ ), respectively, as shown in Figs. 4(c-e). These improvements were consistent with the CRLB improvements in the  $x$  direction by  $1.4\times$ ,  $1.2\times$ , and  $1.4\times$  for each  $z_o$  position in Fig. 3(a). Therefore, it can be concluded that the improved PSF model using cubic spline has led to a  $\sim 1.3\times$  improvement in imaging resolution in the  $x$  direction. Based on the CRLB precision data presented in Fig. 3(a), a similar improvement factor in the  $o$  direction (on average,  $\sim 1.2\times$ ) is expected.

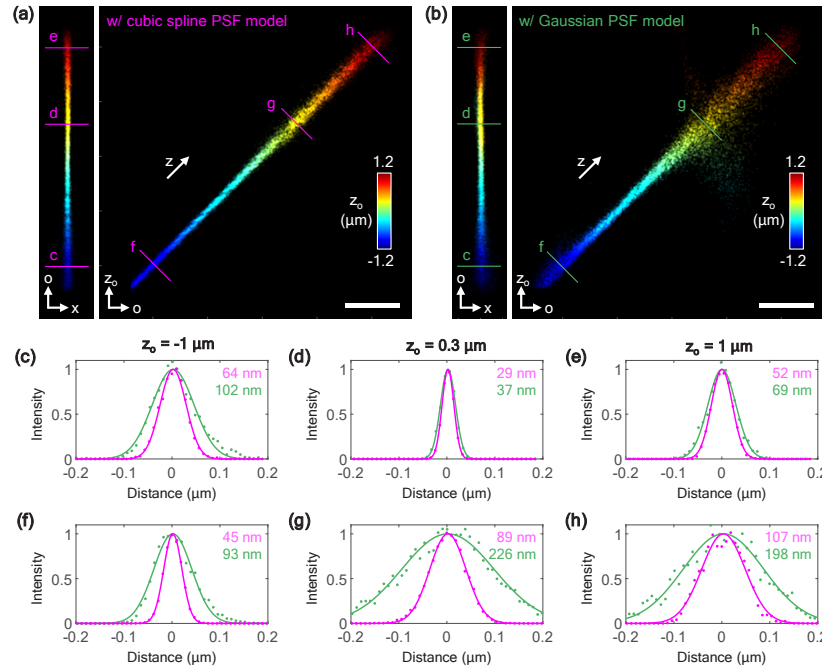


**Fig. 4.** 3D STORM imaging of a dark-red fluorescent bead moving in the  $z$  direction. Line trajectories of the bead reconstructed using (a) cubic spline and (b) Gaussian PSF models. Scale bar:  $500\ \text{nm}$ . (c-h) Cross-sectional intensity profiles for the magenta and green lines shown in panels (a) and (b). The intensity data and their Gaussian fits are displayed as dots and lines, respectively. FWHM linewidths obtained from the fits are displayed as numbers.

As shown in Figs. 4(f-h), the cspline PSF model resulted in significant improvements in the FWHM widths of the intensity cross-sections along the diagonal direction at  $z_o = -1.0$ ,  $0.3$ , and  $1.0\ \mu\text{m}$  in the  $oz_o$  plane, by factors of  $2.1\times$ ,  $2.5\times$ , and  $1.9\times$ , respectively. The corresponding CRLB precision improvements (cspline vs. Gaussian PSF models) were estimated as  $2.0\times$ ,  $4.1\times$ , and  $2.5\times$ , respectively, by root mean square of the CRLB data in  $o$  and  $z_o$  directions in Fig. 3.

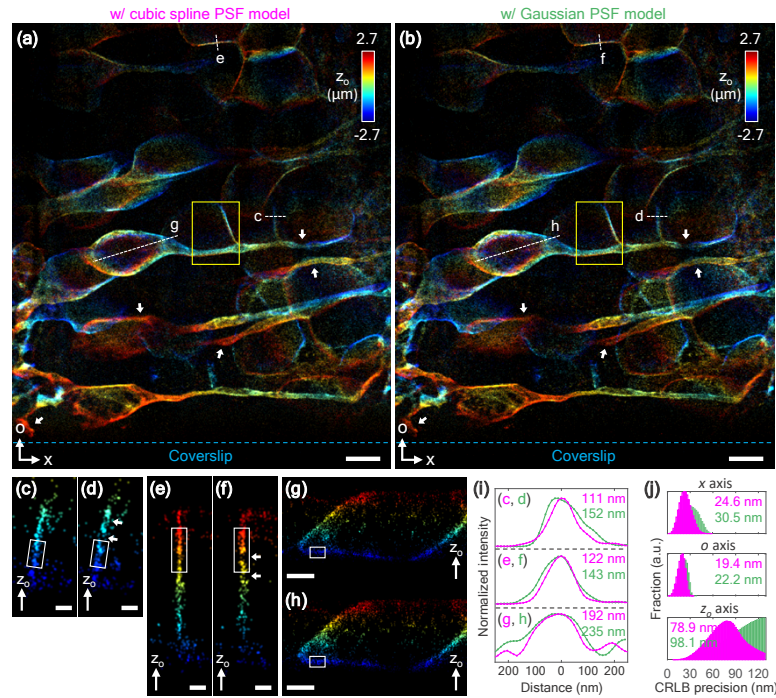


**Fig. 5.** A comparative study of volumetric obSTORM images of PKC $\alpha$  within a mouse retina section, reconstructed using (a) cubic spline and (b) Gaussian PSF models. (c-h) Cross-sectional views along the white dashed lines marked in panels (a) and (b). (i) The cross-sectional intensity profiles at the white boxed regions, projected along the longer direction of the boxes, in panels (c-h). FWHM values are displayed. (j) The histograms of CRLB precision for single molecule data in (a) and (b). The mean precisions in each axis direction are shown. Scale bars: 5  $\mu\text{m}$  (a, b), 500 nm (c-f), and 2  $\mu\text{m}$  (g, h).

While the improvements in FWHM width and CRLB precision were consistent at  $z_o = -1.0 \mu\text{m}$ , the FWHM improvements at  $z_o = 0.3$  and  $1.0 \mu\text{m}$  were not as large as the CRLB improvements. One possible explanation is that at these  $z_o$  positions, some of the localization data from the Gaussian PSF model were overly scattered, and such excessively dispersed molecule data points were not included in the FWHM calculation. The  $\sim 2$ -fold resolution improvement shown in Figs. 4(f-h) was primarily due to the improved localization precision along the  $z_o$  direction. Therefore, it can be said that the cspline PSF model has improved the  $z_o$  resolution approximately two-fold at these  $z_o$  positions, and the entire 2.4  $\mu\text{m}$  range of  $z_o$  could be utilized for 3D localization.

We subsequently evaluated the performance improvements on real tissue samples. As shown in Fig. 5, we reconstructed volumetric STORM images ( $\alpha = 45^\circ$ ) of Alexa Fluor 647-labeled PKC $\alpha$  from a mouse retina slice (using single molecule data from [14]) based on each of the PSF models. The STORM images contained 10 optical sections, captured with a  $z_o$ -step interval of  $\sim 504$  nm. We used only single molecules identified within  $z_o = [-1, 0] \mu\text{m}$  range in each section, with estimated CRLB precisions under 60 nm in  $x_o$  and 130 nm in  $z_o$ , adhering to the same filtering condition as the previous reconstruction [14]. The cspline PSF model provided a more accurate structural reconstruction with increased densities of single molecules at several field locations, as indicated by white arrows in Figs. 5(a) and 5(b). Enhanced image reconstruction was also evident in cross-sectional views at different field locations, as showcased in Figs. 5(c-h). In contrast to the inferior stitching quality between adjacent optical sections (highlighted by

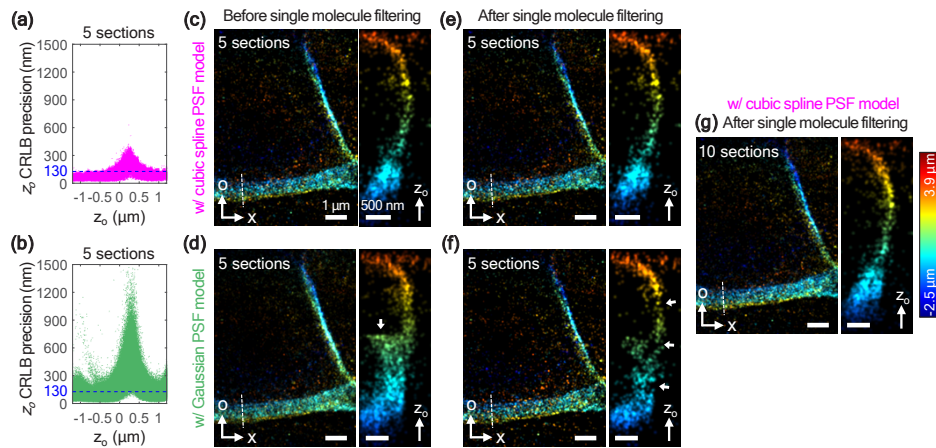


**Fig. 6.** Distributions of CRLB precision in  $z_o$  for data from 5 alternating optical sections of PKC $\alpha$  within a mouse retina slice, as determined by (a) cspline and (b) Gaussian PSF models. (c-f) Volumetric STORM images (corresponding to the yellow-boxed area in Fig. 5) and cross-sectional views along white dashed lines. These images show the effects of single molecule filtering (threshold: 130 nm in  $z_o$  CRLB precision) under each PSF model. (g) The magnified view of the yellow-boxed area in Fig. 5(a) (derived from the complete set of 10 sections) and the cross-sectional view for comparison.

white arrows in Figs. 5(d) and 5(f)) achieved using the Gaussian PSF model, the cspline PSF model produced seamless stitching with continuous intensity outlines of membrane-bound PKC $\alpha$ . Further, as Fig. 5(i) shows, the intensity cross-sections were narrower by factors of 1.37 $\times$ , 1.17 $\times$ , and 1.22 $\times$  in the  $x$ ,  $o$ , and  $z_o$  directions, respectively, when localized using the cspline PSF model. These ratios aligned closely with the improvement ratios of average localization precisions shown in Fig. 5(j), which were ( $x$ ) 1.24 $\times$ , ( $o$ ) 1.14 $\times$ , and ( $z_o$ ) 1.24 $\times$ . These values also corresponded with the average CRLB precision ratios of the calibration bead (cspline vs Gaussian PSF models) in Fig. 3 when averaged over  $z_o = [-1, 0]$   $\mu\text{m}$ , i.e., ( $x$ ) 1.19 $\times$ , ( $o$ ) 1.13 $\times$ , and ( $z_o$ ) 1.28 $\times$ . Thus, it can be concluded that the cspline PSF model enhances image resolution by approximately 1.15-1.25 $\times$  depending on axis directions, when using 1- $\mu\text{m}$ -thick optical section ( $z_o = [-1, 0]$   $\mu\text{m}$ ) with CRLB precision filtering.

Lastly, we evaluated the potential of increasing the  $z_o$  sectioning interval with the cspline PSF model by reconstructing STORM images from only five alternating optical sections (sections 1, 3, 5, 7, and 9) of the mouse retina data in Fig. 5, but now using the full range of each optical section,  $z_o = [-1.2, 1.2]$   $\mu\text{m}$ . As demonstrated in Figs. 6(a) and 6(b), the  $z_o$  CRLB precision of single molecules from these 5 sections mirrored closely the trend of the CRLB precision distribution for the calibration bead shown in Fig. 3(b), showing the worst precision around  $z_o = 300$  nm. By using the cspline PSF model, the average CRLB precision improved significantly by approximately 1.7-fold, decreasing from 154.8 nm (Fig. 6(b)) with the Gaussian model to 91.3 nm (Fig. 6(a)). This considerable improvement led to clearer membrane-like outlines of PKC $\alpha$  in the cross-sectional view (Fig. 6(c)), as opposed to the distorted structure (indicated by the white arrow in Fig. 6(d)) observed when the full  $z_o$  range was applied in the Gaussian PSF model. Upon applying single molecule filtering based on a threshold precision of 130 nm in  $z_o$ , only a small fraction ( $\sim 15\%$  of single molecules) was excluded in the cspline PSF model. Importantly, even when only 5 sections were used, the resulting STORM images exhibited clear and distant outlines of PKC $\alpha$  without discernible stitching artifacts (Fig. 6(e)), maintaining a quality comparable to those reconstructed from the full 10 sections (Fig. 6 g). Conversely, using



the Gaussian PSF model led to a significant data loss, as nearly half (~48%) of single molecules were discarded. This resulted in a fragmented outline of PKC $\alpha$ , indicated by the white arrows in Fig. 6(f), along with incomplete removal of the distorted structure. This result underscores the benefits of using the cspline PSF model, which utilizes the full  $z_o$  range of 2.4  $\mu\text{m}$  and supports at least a two-fold increase in the  $z_o$  interval between adjacent optical sections. Such an enhancement could reduce the image acquisition time in volumetric obSTORM by half.

#### 4. Conclusion

In this study, we have demonstrated the superior accuracy of cubic splines in modeling the through-focus PSF shapes in obSTORM, achieving less than 4% deviation. This refinement offers a more sophisticated PSF model compared to the conventional Gaussian model. Remarkably, this improved model enhances the 3D localization precision, resulting in a substantial improvement in estimated CRLB precisions by 1.1-1.6 $\times$  in  $x_o$  and 1-4 $\times$  in  $z_o$  across the full  $z_o$  range of [-1.2, 1.2]  $\mu\text{m}$ . These enhancements in localization precision have been substantiated by FWHM improvements in scanned bead STORM images, with a factor of 1.3-1.6 $\times$  in  $x_o$  and 1.9-2.5 $\times$  in  $z_o$  at three different  $z_o$  positions.

When applied to single molecule data of real mouse retina tissues, the cubic spline PSF model has improved the obSTORM imaging resolution by an average of 1.15-1.25 $\times$  in all axis directions. Notably, this improvement factor is achieved even when compared against the optimally trimmed resolution in the previous obSTORM reconstruction by limiting the section range to  $z_o = [-1, 0]$   $\mu\text{m}$  (an interval where the Gaussian PSF model performs relatively well) and by aggressively filtering out single molecules with subpar localization precision. Moreover, the cubic spline model enhances the stitching quality of neighboring optical sections in volumetric STORM images of PKC $\alpha$  and allows for a relaxation of the  $z_o$  interval for volumetric obSTORM to at least double when using the full  $z_o$  range of 2.4  $\mu\text{m}$ .

To conclude, our incorporation of the cubic spline PSF model into obSTORM significantly propels the deep-tissue STORM technology forward, enhancing imaging fidelity and expediting volumetric imaging time. This advancement could significantly enhance the capability of super-resolution obSTORM imaging in tissue and small animal studies.

**Funding.** Seoul National University (Creative-Pioneering Researchers Program); National Research Foundation of Korea (No. 2021R1C1C1013067, NRF-2022R1A6A1A03063039).

**Acknowledgments.** The authors thank Dr. Taehwan Kim (University of California, Berkeley) for assistance with cspline PSF modeling. This work was supported by Creative-Pioneering Researchers Program through Seoul National University, the National Research Foundation of Korea (NRF) grant funded by the Korean government (MSIT) (No. 2021R1C1C1013067), and Basic Science Research Program through the National Research Foundation of Korea (NRF) funded by the Ministry of Education (NRF-2022R1A6A1A03063039). This work was in part supported by the Research Institute for Convergence Science. Donghoon Koo acknowledges a fellowship from the Hyundai Motor Chung Mong-Koo Foundation.

**Disclosures.** The authors declare no conflicts of interest.

**Data availability.** Data underlying the results presented in this paper are not publicly available at this time but may be obtained from the authors upon reasonable request.

#### References

1. M. J. Rust, M. Bates, and X. Zhuang, "Sub-diffraction-limit imaging by stochastic optical reconstruction microscopy (STORM)," *Nat. Methods* **3**(10), 793–796 (2006).
2. E. Betzig, G. H. Patterson, R. Sougrat, O. W. Lindwasser, S. Olenych, J. S. Bonifacino, M. W. Davidson, J. Lippincott-Schwartz, and H. F. Hess, "Imaging intracellular fluorescent proteins at nanometer resolution," *Science* **313**(5793), 1642–1645 (2006).
3. S. T. Hess, T. P. K. Girirajan, and M. D. Mason, "Ultra-high resolution imaging by fluorescence photoactivation localization microscopy," *Biophys. J.* **91**(11), 4258–4272 (2006).
4. B. Huang, W. Wang, M. Bates, and X. Zhuang, "Three-dimensional super-resolution imaging by stochastic optical reconstruction microscopy," *Science* **319**(5864), 810–813 (2008).

5. K. Xu, G. Zhong, and X. Zhuang, "Actin, spectrin, and associated proteins form a periodic cytoskeletal structure in axons," *Science* **339**(6118), 452–456 (2013).
6. A. Dani, B. Huang, J. Bergan, C. Dulac, and X. Zhuang, "Superresolution imaging of chemical synapses in the brain," *Neuron* **68**(5), 843–856 (2010).
7. F. Herrmannsdörfer, B. Flottmann, S. Nangner, V. Venkataramani, H. Horstmann, T. Künér, and M. Heilemann, "3D d STORM imaging of fixed brain tissue," in *Synapse Development: Methods and Protocols*, A. Pouloupoulos, ed. (Springer New York, 2017), pp. 169–184.
8. F. Cella Zanacchi, Z. Lavagnino, M. Perrone Donnorso, A. Del Bue, L. Furia, M. Faretta, and A. Diaspro, "Live-cell 3D super-resolution imaging in thick biological samples," *Nat. Methods* **8**(12), 1047–1049 (2011).
9. J. C. M. Gebhardt, D. M. Suter, R. Roy, Z. W. Zhao, A. R. Chapman, S. Basu, T. Maniatis, and X. S. Xie, "Single-molecule imaging of transcription factor binding to DNA in live mammalian cells," *Nat. Methods* **10**(5), 421–426 (2013).
10. R. Galland, G. Greci, A. Aravind, V. Viasnoff, V. Studer, and J.-B. Sibarita, "3D high- and super-resolution imaging using single-objective SPIM," *Nat. Methods* **12**(7), 641–644 (2015).
11. F. Greiss, M. Deligiannaki, C. Jung, U. Gaul, and D. Braun, "Single-molecule imaging in living drosophila embryos with reflected light-sheet microscopy," *Biophys. J.* **110**(4), 939–946 (2016).
12. M. B. M. Meddens, S. Liu, P. S. Finnegan, T. L. Edwards, C. D. James, and K. A. Lidke, "Single objective light-sheet microscopy for high-speed whole-cell 3D super-resolution," *Biomed. Opt. Express* **7**(6), 2219–2236 (2016).
13. A.-K. Gustavsson, P. N. Petrov, M. Y. Lee, Y. Shechtman, and W. E. Moerner, "3D single-molecule super-resolution microscopy with a tilted light sheet," *Nat. Commun.* **9**(1), 123 (2018).
14. J. Kim, M. Wojcik, Y. Wang, S. Moon, E. A. Zin, N. Marnani, Z. L. Newman, J. G. Flannery, K. Xu, and X. Zhang, "Oblique-plane single-molecule localization microscopy for tissues and small intact animals," *Nat. Methods* **16**(9), 853–857 (2019).
15. H. P. Babcock and X. Zhuang, "Analyzing single molecule localization microscopy data using cubic splines," *Sci. Rep.* **7**(1), 552 (2017).
16. Y. Li, M. Mund, P. Hoess, J. Deschamps, U. Matti, B. Nijmeijer, V. J. Sabinina, J. Ellenberg, I. Schoen, and J. Ries, "Real-time 3D single-molecule localization using experimental point spread functions," *Nat. Methods* **15**(5), 367–369 (2018).
17. J. Ries, "SMAP: a modular super-resolution microscopy analysis platform for SMLM data," *Nat. Methods* **17**(9), 870–872 (2020).
18. M. Bates, J. Keller-Findeisen, A. Przybylski, A. Hüper, T. Stephan, P. Ilgen, A. R. Cereceda Delgado, E. D'Este, A. Egner, S. Jakobs, S. J. Sahl, and S. W. Hell, "Optimal precision and accuracy in 4Pi-STORM using dynamic spline PSF models," *Nat. Methods* **19**(5), 603–612 (2022).